Highlights

Impacting the dayside Martian ionosphere from above and below: Effects of the impact of CIRs and ICMEs close to aphelion (April 2021) and during dust storms (June/July 2022) seen with MAVEN ROSE

Marianna Felici, Jennifer Segale, Paul Withers, Christina O. Lee, Andrea Hughes, Ed Thiemann, Steve Bougher, Candace Grey, Shannon Curry

- Increase in TEC up to 2.5×10^{15} m^{-2} in the Martian ionosphere between 80 and 300 km following an ICME/CIR impact.
- Increase in TEC up to 5×10^{15} m^{-2} in the Martian ionosphere between 80 and 300 km following ICME/CIR impacts during dust storms.
- During dust storms, the peak altitudes of the Martian ionospheric layers M1 and M2 loft of the same amount.

Impacting the dayside Martian ionosphere from above and below: Effects of the impact of CIRs and ICMEs close to aphelion (April 2021) and during dust storms (June/July 2022) seen with MAVEN ROSE

Marianna Felici[a], Jennifer Segale[b], Paul Withers[c], Christina O. Lee[d], Andrea Hughes[e], Ed Thiemann[f], Steve Bougher[g], Candace Grey[h], Shannon Curry[i]

[a]*Center for Space Physics, Boston University, 725 Commonwealth Avenue, Boston, MA, USA*
[b]*Department of Astronomy, Boston University, Boston, MA, USA*
[c]*Department of Astronomy, Boston University, Boston, MA, USA*
[d]*Space Science Laboratory ,University of California, Berkeley, CA, USA*
[e]*NASA Goddard Space Flight Center, Greenbelt, MD, USA*
[f]*LASP, University of Colorado, Boulder, BO, USA*
[g]*University of Michigan, Ann Arbor, MI, USA*
[h]*NMSU Astronomy Department, Las Cruces, NM, USA*
[i]*LASP, University of Colorado, Boulder, CO, USA*

Abstract

We use 62 electron density profiles collected by the Radio Occultation Science Experiment (ROSE), on the Mars Atmosphere and Volatile EvolutioN (MAVEN), when Mars was hit by CIRs and ICMEs close to aphelion (April 2021) and during two dust storms (June/July 2022) to examine the response of the Martian ionosphere to solar events and to solar events hitting during dust storms. We do so through three proxies – variation in total electron content between 80 and 300 km altitude, peak density, and peak altitude – of the aforementioned 62 ROSE electron density profiles, relative to a characterisation of the ionosphere through so-

lar minimum leading to solar maximum, specific to local time sector and season, presented in the https://arxiv.org/abs/2312.00734 by Segale et al., [https://arxiv.org/abs/2312.00734]. We observe an increased Total Electron Content (TEC) between 80 and 300 km altitude up to $\simeq$ 2.5 $\times 10^{15}$ m^{-2} in April 2021 and up to $\simeq$ 5 $\times 10^{15}$ m^{-2} in June/July 2022 compared to the baseline photochemically produced ionosphere. This increase in TEC corresponds mainly to increases in the solar energetic particles flux (detected by MAVEN Solar Energetic Particle, SEP) and electron fluxes (detected by the MAVEN Solar Wind Electron Analyzer, SWEA). In addition to solar events, in June/July 2022, an A storm and a B storm were occurring and merging on the surface of Mars. We observe a raise in peak altitude in general lower than expected during dust storms, possibly due to high values of solar wind dynamic pressure (derived from MAVEN Solar Wind Ion Analyzer, SWIA). From 31 ROSE profiles collected in this time period that showed both the M2 and M1 layer, we observe that, on average, M1 and M2 peak altitudes raise the same amount, suggesting that the thermosphere might loft as a unit during dust storms. During this time period, several proton aurora events of variable brightness were detected with MAVEN Imaging Ultraviolet Spectrograph (IUVS), underlining the complex and multifaceted impact of dust activity and extreme solar activity on the Martian ionosphere.
Keywords: CME, SIR, CIR, Dust, Mars, Ionosphere

1. Introduction

At Mars, the ionisation in the dayside ionosphere, a region of the atmosphere embedded in the thermosphere, is mainly controlled by photochemical

processes such as CO_2 + photon $\rightarrow$ CO_2^+ + e, CO_2^+ + O $\rightarrow$ O_2^+ + CO, O_2^+ + e $\rightarrow$ O + O) below about 170-200 km. At those altitudes, in fact, photochemical processes act faster than plasma transport (e.g. Barth et al., 1992; Fox, 2004; Withers, 2009; Bougher et al., 2017) and the behaviour of the peak densities as a function of solar flux and of solar zenith angle can generally be represented quite well by the idealised photochemical theory for both the M2 layer (created by EUV radiation) and M1 layer (created mainly by X-rays radiation and secondary electrons) (Chamberlain and Hunten, 1987; Withers, 2009).

Mars is immersed in the heliosphere and, therefore, is subject to space weather and solar events. For example, the interaction between the stream of faster solar wind originating from solar coronal holes and the stream of preceding slower solar wind forms a region of compressed plasma, the stream interaction region (SIR). If the SIR, twisted into a spiral by the rotation of the Sun, persists for more than one solar rotation, then it is referred to as Corotating Interaction Region (CIR) (Richardson, 2018, and references therein). The in situ signatures associated with SIRs and CIRs can be enhancements in the solar wind dynamic pressure; solar wind particle speed and density; frequent pure energetic ion enhancements, namely no enhancement in the flux of energetic solar wind electrons, but only in the flux of ion with energies $\sim$ MeV/n); less frequent pure electron enhancements ($\sim$ 0.04 - 1 MeV); enhancements in both energetic ion and electron; and increase in solar wind magnetic field strength (Richardson, 2018, and references therein).

Another example of solar events are coronal mass ejections (CMEs) which, instead, are bubbles made of billions of tons of solar plasma, with embedded

magnetic fields, that erupt from the Sun and travel outwards in the Interplanetary heliosphere (ICME) at a pace between 250 and 3000 km/s (Jones et al., 2020, and references therein). There are a plethora of in situ signatures in the interplanetary medium associated with a CME, depending on whether the CME belongs to the magnetic cloud or non-cloud events categories, and if it is a fast or slow event (Owens, 2018). These signatures do not appear necessarily at the same time, nor in the same region of the heliosphere (Zurbuchen and Richardson, 2006; Owens, 2018); some of these, at 1 AU, can be rotation and enhancement of the magnetic field, forward shock, increase in the α to protons ratio, high energy particles (Zurbuchen and Richardson, 2006). The latter, Solar Energetic Particles (SEPs) (energies in the keV–GeV) can increase in flux: these events can last from hours to days in a large range of heliolongitudes from the Sun (Palmerio et al., 2021) and be associated also to flare events.

Previous studies reported the response of the Martian atmosphere to such events mostly focusing on either the top or the bottom of the ionosphere.

Regarding the effects of CIRs, Dubinin et al. (2009) showed that the impact of a dense and high pressure solar wind can penetrate the Martian induced magnetosphere and induce erosion channels in the ionosphere above 300 km. Edberg et al. (2010), in a statistical study that confirms the findings of previous case studies (e.g., Dubinin et al., 2009), finds that pressure pulses, whether from CIRs or ICMEs, lead to an increase in ions lost from the planet. Ram et al. (2023) suggest that the impact of CIR on the Martian ionosphere is larger compared to CME impacts in a declining phase of the solar cycle.

Ulusen et al. (2012) studied the effect of multiple Solar Energetic Parti-

cles (SEP) events impacting the ionosphere of Mars and found that in some instances the electron density between 100 and 200 km altitudes did not show any increase, however, some of those events did show an increase in density below 100 km altitude, suggesting that superthermal electrons (10−20 keV) could increase ionization below the M1 layer (lower ionosphere); fewer events at limited solar zenith angles, instead, show lower electron density between 100 and 120 km altitude or even at the top of the ionosphere, suggesting that SEP increase atmospheric loss and ionospheric compression. Sánchez-Cano et al. (2019) found solar energetic electron precipitation to be responsible for creating a low ionospheric plasma layer at ∼90 km altitude on the Martian nightside, layer that might have cause days long blackouts in the Mars Advanced Radar for Subsurface and Ionosphere Sounding (MARSIS) onboard Mars Express and the Shallow Radar (SHARAD) onboard the Mars Reconnaissance Orbiter. Lester et al. (2022) found clear correlation between the blackouts of MARSIS and SHARAD instruments and solar cycle, and estimated that, to cause blackout in both instruments, the average SEP energy spectrum is above 70 keV.

Opgenoorth et al. (2013) found that increases in the dynamic pressure of the solar wind would trigger compression in the magnetosphere and ionosphere and, as a consequence, increase plasma transport over the terminator and ion escape. Morgan et al. (2014), also, observed that the ionosphere after an ICME impacting Mars extends well beyond the terminator, up to solar zenith angle of 115°, with a few possible causes such as the increased plasma transport from the dayside, electron precipitation, and increased solar energetic particles precipitation.

The effect of an ICME on the upper atmosphere was also reported by Jakosky et al. (2015a), who observed changes in bow shock and magnetosheath, aurora formation, and enhancement in the pick-up ions population with MAVEN instruments.

From all events that have an impact on the Martian ionosphere from below, we focus on this work on dust Leovy (2001); Kahre et al. (2017), that can have dramatic effects in elevating the altitude of the main ionospheric peaks more than $\sim$ 15 km even if the dust storm is not global to the whole planet (Felici et al., 2020). Withers et al. (2018), in an earlier analysis of MAVEN ROSE observation during a small dust event, found that the dayside ionospheric peak altitudes were enhanced by more than $\sim$ 9 km at 52°N in response to said small dust event. As far as previous large radio occultation datasets, Mars Global Surveyor (MGS) acquired 5600 ionospheric electron density profiles, but these observation were confined at high northern latitudes ($>$ 60° N) and had unfortunate seasonal biases in their coverage. However, Withers and Pratt (2013) identified an instance in Mars Year (MY) 27 where ionospheric peak altitudes observed at 70°N increased by a highly-uncertain 5 km, coincident with a small increase of the dust content of the tropical atmosphere.

Girazian et al. (2019) studied dust events during six different Mars Years (MY) using data from the MARSIS (Mars Advanced Radar for Surface and Ionosphere Sounding) instrument on Mars Express. They report an increase $\sim$10–15 km during all six event, regardless of whether these were local, regional, or global storms.

The aim of this article is to utilise the baseline for the ionosphere through

solar minimum leading to solar maximum provided by the work of Segale et al., [https://arxiv.org/abs/2312.00734] to separate solar events and dust effects on the Martian ionosphere from the baseline photochemically produced Martian ionosphere. We do this for altitudes between 80 and 300 km, when the Martian ionosphere is impacted by CIRs and ICMEs, during aphelion season, defined here as the ranges 0-161° and 341-360° L_S, non-dust season; and perihelion season, defined here as the range 161-341° L_S, which corresponds to dust season, during two merging dust storms. To achieve our aim, we utilise electron density profiles from the MAVEN Radio Occultation Science Experiment (ROSE) (Withers et al., 2020), from which we define three proxies: variation from the baseline ionosphere of total electron content, peak density, and peak altitude.

The structure of this article is as follows: Section 2 describes the observations analysed in this work and the methodologies with which these were analysed. Section 3 reports and interprets MAVEN ROSE observations obtained during ICMEs and CIRs impacts collected in 2021 and 2022. Section 4 summarises the findings of this work.

2. Methods

The Radio Occultation Science Experiment (ROSE) (Withers et al., 2020) has been part of the scientific payload of the Mars Atmosphere Volatile EvolutioN (MAVEN) spacecraft (Jakosky et al., 2015b) since 2016. ROSE conducts two-way X-band radio occultations, providing seasonal observations of the vertical structure of the ionosphere, including the main plasma layer and below. That region of the ionosphere ($\sim$ 130 km and below) has rarely been

accessible to other in situ instruments on MAVEN. ROSE has collected more than 1000 electron densities profiles since 2016, with global geographical coverage ($\sim$ -85 to 89° in latitude and $\sim$ -180 to 180° in longitude) and broad Solar Zenith Angle (SZA) coverage ($\sim$ 47 to 136°).

To evaluate the effects that ICMEs and CIRs impacts have on the ionosphere of Mars, and separate them from the baseline photochemical ionosphere, between 80 and 300 km altitude, both when the ionosphere is otherwise undisturbed and when it is, instead, heated by the presence of dust and additionally lofted from below by dust storm, we restricted this study to time intervals for which we had a series of ROSE electron density profiles that broadly covered the dayside ionosphere (SZA $< 95°$).

We selected two time periods during which the ionosphere of Mars is impacted by CIRs and/or ICMEs:

1. **April 2021**: we utilised 21 ROSE electron density profiles collected between April 9th and April 23rd 2021. These profiles cover a range in SZA between $\simeq$ 71 and 94°. As for Local Solar Time (LST), all the profiles were collected consistently in the afternoon at $\simeq$ 16:00, and, latitudinally, in the southern hemisphere; the longitudinal sampling is homogeneous. L_S in this time interval ranges between 29 and 36°, therefore we are close to aphelion (defining aphelion here as the ranges in L_S 0-161° and 341-360°). While we do have MAVEN in situ measurements for this time period, MAVEN was not upstream from Mars, therefore determining the exact ICME and CIR arrival times is not possible. However, Dresing et al. (2023) report about a long-lasting solar eruption on 17 April 2021 which generated a Solar Energetic Particle

(SEP) event so widespread that was detected by different observers in the heliosphere (see Dresing et al. (2023), Figure 14, for Mars). We report MAVEN Solar Wind Electron Analyzer (SWEA (Mitchell et al., 2016)) and Solar Energetic Particle (SEP) data (Larson et al., 2015) in Figure Appendix .11, and in Figure 3: we see a first peak in particle flux around April 12th-13th, one around the 19th, and another, larger, on the 22nd.

2. **June/July 2022**: We utilised 41 ROSE electron density profiles collected between June 13th and July 22th 2022. These profiles cover a SZA range between $\simeq$ 47 and 95° - very broad coverage and the lowest in SZA ROSE had ever gotten - spanning nearly the entire dayside range permitted by radio occultation geometry. As for LST, most of these profiles span from $\sim$ 01:00 until 09:00 LST, therefore mostly dawn sector/noon, and 11 of these were collected at dusk after $\sim$ 2300. Latitudinally, all profiles were collected in the southern hemisphere (see Figure 1). L_S spanned in this time interval ranges between 246 and 271°, therefore we are at perihelion, in full dust season. Not only that, but, at this time, there were two dust storm merging at Mars, below the ionosphere: an A class storm ('a classic regional-scale or planet encircling Southern Hemisphere dust event' Kass et al. (2016)) which started on May 2nd, at $\sim$ 219 L_S, peaked at $\sim$ 227 L_S, and ended at $\sim$ 259 L_S; and a B class storm ('southern polar event' Kass et al. (2016)), which started on June 28th, at $\sim$ 255 L_S, peaked at $\sim$ 265 L_S, and ended at $\sim$ 298 L_S. In Figure 1 we show ROSE data coverage in this time period, overlapped with the normalised IR absorption (Montabone

et al., 2015, 2020): ROSE data crossed the two storms fully. Between ∼250 and 260° L_S some ROSE data is located at latitudes outside the dustiest areas (see Figure 1); however, the timescale with which the thermosphere recovers from dust effects can range between 20 and 120° L_S (Withers and Pratt, 2013), therefore these profiles can still be considered affected by dust. While we do have MAVEN in situ measurements for this time period as well (see Figure Appendix .12 and 6), MAVEN did not sample the upstream solar wind conditions until July 6th 2022 (see Figure Appendix .13, (Halekas et al., 2015; Halekas et al., 2017, 2015)), bottom three panels), therefore determining the exact ICMEs/CIRs arrival time is not possible. However, we do see a large increase in SEP fluxes starting around July 12th and culminating on July 13th/14th, and smaller ones at the end of June/beginning of July.

We use the simulation results of the modelled ICME propagation and ambient solar wind conditions produced from the ENLIL heliospheric solar wind model (Odstrcil, 2003), given that during both these time periods Earth and Mars were located at $\leq 90°$ from each other on the ecliptic plane (see Figure Appendix .11 and Appendix .12). The model has limitation and uncertainties ($\sim$ 24 hours at Mars for both shock arrival time and ejecta arrival time (Palmerio et al., 2021)), for example given by the choice of input of the CME injection direction, time, size, and shape (Lee et al., 2018, and references therein), however, ENLIL has been found to be a good first order approximation of the heliospheric conditions associated with the CME (e.g. Palmerio et al., 2021).

For this study, we use the ENLIL simulation results for obtaining a more global context of interplanetary conditions at Mars, and, as a tool for interpreting the in situ MAVEN measurements during space weather activity, particularly when the spacecraft was not located upstream, i.e., outside the Martian bow shock, to directly observe the SIR/CIR or ICME impacts (e.g., Lee et al., 2018, and references therein). The ENLIL simulation results are publicly available through the NASA Community Coordinated Modeling Center (CCMC) Space Weather Database Of Notifications, Knowledge, Information (DONKI) website `https://kauai.ccmc.gsfc.nasa.gov/DONKI/search/`.

We report in Figures Appendix .11 and Appendix .12 particles and field data and ENLIL images for these two time periods.

Based on the ENLIL simulation results, in April 2021, the first increase in particle flux might be due to a CIR impacting Mars around April 11th, the second to a glancing blow from a ICME impacting Mars on April 18th, the third to a direct ICME impact on Mars on April 22nd (Figure Appendix .11).

In June/July 2022, based on the ENLIL simulation results, there may have been an ICME impact at Mars on June 18th and a glancing blow ICME impact combined with a CIR on June 24th, and ICME with glancing blow on July 2nd, a ICME on July 13th, and a glancing blow from a ICME combined to a CIR on July 14th (Figure Appendix .12).

We identified three quantities that could help us evaluate the effects of these different drivers on the ionosphere and quantify the deviation that these induce from the undisturbed photochemically produced ionosphere: the Total Electron Content (TEC) between 80 and 300 km altitudes (as above 300 km

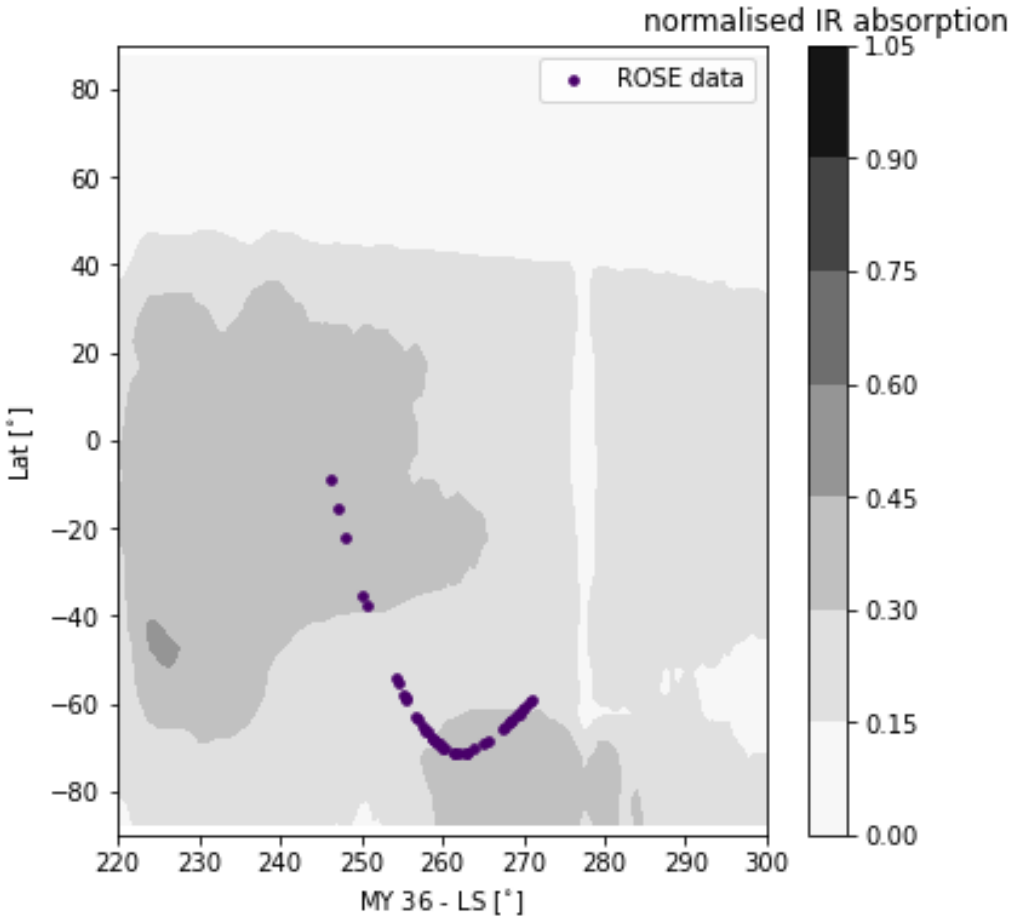

Figure 1: June/July 2022: ROSE data coverage overlapped with a dust map obtained from the Mars Climate Database (Montabone et al., 2015, 2020).

the plasma population could instead be depleted by the Solar Wind (SW) (Dubinin et al., 2009)); the peak electron density, which normally in the dayside coincides with the M2 peak density; and the peak altitude, namely the altitude at which we have highest electron density, which, normally in the dayside tends to coincide with the M2 peak altitude.

To quantify the effects that space weather events and dust storm induce on the ionosphere, we need to isolate and subtract the baseline photochemically produced ionosphere first. In order to do this accurately, our baseline photochemically produced ionosphere must account for changes that solar local time and season induce on the ionosphere, because these also play a role [Segale et al., https://arxiv.org/abs/2312.00734]. We report here summary and conclusions from Segale et al., [https://arxiv.org/abs/2312.00734] *"219 electron density profiles of the Martian undisturbed dayside ionosphere collected by MAVEN ROSE between July 2016 and December 2022 through solar minimum leading to solar maximum, show clear M2 and M1 layers. We used these 2019 profiles to characterise how M2 and M1 peak electron densities and altitudes change with SZA, LST sector - dawn vs dusk - and season – aphelion (Southern Autumn and Winter) vs perihelion (Southern Spring and Summer). Therefore, we split these 219 profiles in four groups: dawn aphelion, dawn perihelion, dusk aphelion, and dusk perihelion. We find distinct differences between the different groups of data. The biggest difference, both in peak densities and in peak altitudes, is found between dawn perihelion and aphelion, consistently with the hypothesis of a more variable dawn ionosphere (Felici et al., 2022). For both the M1 and M2 layers, dawn perihelion is significantly higher in altitude and greater in density than dawn aphelion. For*

dusk aphelion and perihelion the difference is usually less extreme. Dusk perihelion is higher in density than dusk aphelion, but dusk aphelion is higher in altitude, particularly in the M1 layer. Densities and altitudes of the M1 and M2 layers generally tend to be higher at perihelion, expected since when Mars is closer to the Sun, we expect higher solar flux to irradiate the atmosphere. However, densities and altitudes are lower than what Fallows et al. (2015) found, at solar maximum. Namely, corresponding to the solar minimum in the solar cycle, we find lower peak densities and lower peak altitudes for both the M1 and M2 layers. Finally, as SZA increases the M1 and M2 peaks get farther in altitude from one another, yet closer in density". Therefore, we utilised a novel approach in this study, and fully leveraged the parameters estimated by Segale et al., [https://arxiv.org/abs/2312.00734] to model the baseline electron density profiles from mere photochemical reactions, and subtract that baseline from our data. To so do, we estimated TEC, peak density, and peak altitude for two different sets of electron density profiles, namely:

SET A The series of measured ROSE electron density profile collected during time periods 1 (**April 2021**) and 2 (**June/July 2022**). An example of a measured electron density profile during period 2, affected by CIRs, ICMEs, and dust storms, is reported in Figure 2, in purple.

SET B A series of modelled electron density profiles generated from eq. 2 in Fallows et al. (2015), accounting from SZA dependence of the M2 and M1 peak densities and altitudes through their eq. 3 and 5. These equations are reported here as Equations 1, 2, 3, and 4. The peak

altitudes of the M1 and M2 layers follow

$$z_m = z_0 + L \times ln(\sec(SZA)) \tag{1}$$

where m stands for either the M1 or the M2 peak, z_m is the altitude of the peak, z_0 is the sub-solar altitude of the peak, SZA is Solar Zenith Angle, and L is the lengthscale which should coincide with the scale height of the neutral atmosphere, where the idealised photochemical theory applies. The peak densities of the M1 and M2 layers, instead, follow

$$N_m = N_0(\frac{1}{\sec(SZA)})^k \tag{2}$$

N_m is the density of the peak, N_0 is the sub-solar density of the peak, and k is the fitted exponent. For an idealised photochemical theory

$$N_{tot} = N_{m1} + N_{m2} \tag{3}$$

Which leads to

$$N(z, sza) = \sum N_m exp(\frac{1}{2}(1 - \frac{z - z_m}{L_m} - exp(-\frac{z - z_m}{L_m}))) \tag{4}$$

As values for z_0, L_m, N_m, and k we utilised the fit parameters obtained by Segale et al. [https://arxiv.org/abs/2312.00734] and reported in their Tables 2 and 3, for appropriate SZA, and four different combination of Local Time Sector and L_S range: dawn aphelion, dawn perihelion, dusk aphelion, and dusk perihelion. We so obtained N_m and z_m, and, finally, N. Segale et al. [https://arxiv.org/abs/2312.00734], in fact, not only identified the baseline for the variations in peak altitude and density of the M1 and M2 layers as a function of SZA from ROSE

profiles of an undisturbed ionosphere at solar minimum [see Segale et al., https://arxiv.org/abs/2312.00734], but they separated these trends into dawn (00:00 till 12:00 LST) and dusk (12:00 till 24:00 LST) sectors, and aphelion and perihelion season. As a reminder, aphelion and perihelion season are defined respectively as the intervals 0-161° and 341-360° L_S, and 161-341° L_S. Therefore, in this study, we were able to generate modelled electron density profiles for each of the profile in SET A, and account for their SZA, whether it was collected at dusk or at dawn, and if that was during perihelion or aphelion season. An example of a so modelled electron density profile - of the merely photochemically produced undisturbed ionosphere - is reported in Figure 2, in green: this is the modelled profile at the same SZA, local time sector, and season, as the corresponding measured profile (Figure 2, in purple).

Finally, we calculated the difference between TEC, peak density, and peak altitude of the profiles in **SET A** and TEC, peak density, and peak altitude of the profiles in **SET B** and obtained the three proxies ΔTEC, Δ(Peak Density), Δ(Peak Altitude). In other words, ΔTEC, Δ(Peak Density), Δ(Peak Altitude) constitute the deviation of TEC, peak density, and peak altitude induced by space weather and dust storms from the baseline photoproduced ionosphere. Besides being independent from SZA, LST sector, and season, these three proxies would be equal to 0 in undisturbed times for the ionosphere, namely times Segale et al., [https://arxiv.org/abs/2312.00734] explored in their study. We report the proxies and how they were derived in Figure 2.

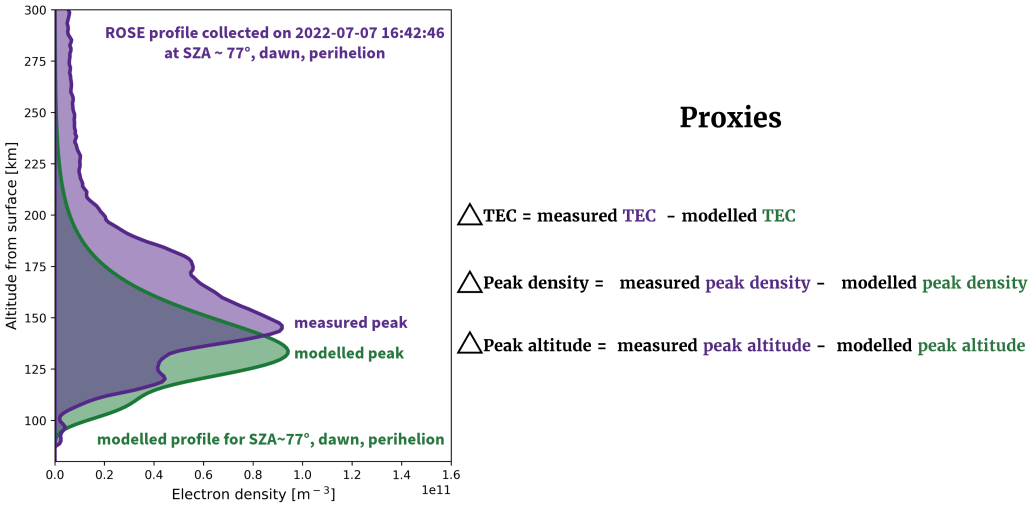

Figure 2: Example of a measured ROSE electron density profile (left, in purple), during July 2022, when the ionosphere of Mars was hit by drivers CIR, ICME, and dust storm. We report the corresponding modelled electron density profile - for a merely photochemically produced undisturbed ionosphere [Segale et al., https://arxiv.org/abs/2312.00734] - with same SZA, LST sector, and season (left, in green). The deviation of the measured profile from a photochemical ionosphere is visible. The three proxies derived from the TEC, peak altitude, and peak densities for sets of profiles A and B are reported on the right: these will will help us quantify the deviation induced by drivers from the undisturbed photochemically produced ionosphere.

Since one of the two events was collected during 2021, approaching conjunction, to all the electron densities in all the profiles we attributed a maximum error of 1.5×10^{10} m^{-3} (Withers et al., 2020), and the errors propagated accordingly. For the error associated to the TEC values, instead, we considered the difference between two different integration methods, one merely given by the manual integration of density values in altitude, one that utilises the Simpson method.

These three proxies from ROSE data were qualitatively compared to the trends of MAVEN calibrated L2 in situ key parameters (on the PDS) for SWEA (total flux of 1 - 500 eV and 500-1000 eV) (Mitchell et al., 2016), SEP (total flux for ions and electrons) (Larson et al., 2015), and dynamic pressure, from Solar Wind Ion Analyzer (SWIA) (Halekas et al., 2015). In future work, we will conduct statistical studies on ICMEs impacting the ionosphere, and, to obtain meaningful quantitative information, utilising subsequent versions of the data for each instrument will be most appropriate, for it contains more accurate and recent quality flags. For the qualitative purpose of this study, the key parameters were a valuable resource instead.

To compare the different time series from in situ and remote instruments, and to identify the time delay between related events, we started from times of detection of the ROSE electron density profiles, and estimated backward time-lagged crossed correlation between ROSE derived proxies and Solar Wind (SW) particle parameters and irradiance. Time-lagged cross-correlation is a statistical technique used to measure the similarity between two whole (not just minima and maxima) time-series while considering a time delay or lag between them. We considered lag = 0 hours/days between

ROSE (y) and in situ (x), backward lag = 12hours/1day (MAVEN in-situ time series shifted -12 hours/-1 day from ROSE proxies), and backward lag = 24hours/2days (in-situ time series shifted -24 hours/-2 days from ROSE proxies). The cross-correlation function is computed for these three different time lags, so we could better visualise the similarity between the two time series at each lag. In other words, the cross-correlation function of x (in-situ solar wind particle parameters) and y (our ROSE derived proxies) is a matrix: the element at index k (the lag) in the resulting array is the correlation between x[k], x[k+1], ..., x[n] and y[0], y[1], ..., y[m-k], where n and m are the lengths of x and y, respectively. A positive value of cross correlation indicates a positive correlation - in other words, similar trend in the two time series, while a negative value suggests a negative correlation - or opposite movement of the two time series under examination. A value of zero means no correlation or similarity. In order to estimate the time-lagged crossed correlation, because the datasets did not have the same cadence, data had to be binned in 12 and 24 hours bins and the mean in each bin of the MAVEN in-situ and remote datasets had to be estimated. 6 h bins led to a $-0.1 <$ correlation < 0.1, larger than 24 h bins would have led to lose information on faster similarities.

The time period June/July 2022, offer the unique opportunity of observing the behaviour of both the M1 and M2 layers in response to the A and B storm that were merging below the ionosphere at this time: we investigate whether of not the M1 and M2 layers are lofted together and if the response of the ionosphere to CIR and/or ICME changes if dust storms are lofting the ionosphere from below.

We report and discuss the results of this methodology in the next Section (3).

3. Results and discussion

3.1. April 2021: CIR and ICME impact at aphelion

As mentioned in Section 2, this time interval is covered by 21 ROSE electron density profiles collected between April 9th and April 23rd 2021. These profiles span a range in SZA between $\simeq$ 71 and 94° and were collected close to aphelion. During this time period, based on the ENLIL simulation results available on the Space Weather Database Of Notifications, Knowledge, Information (DONKI) catalog, in April 2021, the first increase in particle flux might be due to a CIR impacting Mars around April 11th, the second to a glancing blow from an ICME impacting Mars on April 18th, the third to a direct ICME impact on Mars on April 22nd (Figure Appendix .11, and we report the timings for these modelled impacts at the top on Figure 3). In Figure 3, we report the three proxies estimated from ROSE parameters, namely ΔTEC, Δ(Peak Density), and Δ(Peak Altitude) (we want to remind the reader that these proxies are independent from SZA, LST sector, L_S sector); the Solar Wind (SW) dynamic pressure estimated through the SWIA instrument on MAVEN; the SWEA flux measurements the particle energy ranges 100-500 and 500-1000 eV; and the SEP meaurements for ions (energy 30-1000 keV), and SEP electrons (30-300 keV). Follow SWEA and SEP in the panels below.

The first proxy shown in Figure 3, top panel, is the ΔTEC: many of the profiles show a larger TEC than the expected values. For times around April

11th, this corresponds to a larger peak density as well (Figure 3, second panel), anyway consistent with 0 within error. ΔTEC reaches values of $\simeq$ 2.5 $\times 10^{15}$ m^{-2} on April 22nd, and $\simeq$ 2 $\times 10^{15}$ m^{-2} on April 19th without any striking enhancement in Δ(Peak Density) or Δ(Peak Altitude). Therefore, the additional ionisation enhancing the ΔTEC must be occurring altitudes different from that of the main peak, as precipitating particles and EUV radiation are different phenomena. In fact, Nakamura et al. (2022) estimated that 1 keV electrons can ionise CO_2 down to 120 km altitude, therefore particles detected by the SWEA instrument should be responsible only for ionisation - besides the usual photochemical ionisation - at and above the main ionospheric peak. Nakamura et al. (2022) also estimated that electrons above 50 keV and protons with energy 500 keV - where both these energies can be measured by MAVEN SEP - can ionise CO_2 deeper in the atmosphere, down to 80 km altitude, with CO_2^+ production rates 2-3 order of magnitudes larger than that produced by 1 keV electrons.

We report the original ROSE electron densities profiles for this time interval in Figure 4, left, with colourscale representing the SZA of the profiles: these are really disturbed and noisy electron density profiles, possibly due to the vicinity with Mars solar conjunction Withers et al. (2020). In general, the expected behaviour consistent with an idealised photochemical theory - smaller densities with SZA, higher peak altitudes with SZA - can be appreciated, however with the presence of bulkier plasma content at lower altitudes (below 100 km) for a few of these profiles: MAVEN SEP shows an increase in flux of the Solar Energetic Particles (SEPs), able to produce plasma layers below $\sim$ 90 km altitude (Sánchez-Cano et al., 2019; Peter et al., 2021;

Lester et al., 2022; Harada et al., 2023). Additionally, these profiles tend to display a rather extended and spread in altitude ionosphere and, wider-than-the-baseline ionospheric layers (see Figure 4, right, comparison between the measured profile and the modelled), indicating more ionisation than that only due to photoionisation, possibly due to an interplay of increased compression and precipitating particles from the SW: as the high pressure causes the solar wind to get into the ionosphere (Dubinin et al., 2009), solar particles at various energies can penetrate down to various altitudes getting not only down to 80 km (Ulusen et al., 2012; Sánchez-Cano et al., 2017), but to the ground (Zeitlin et al., 2018; Ehresmann et al., 2018). Another rather striking feature shown by these proxies is the suppressed Δ(Peak Altitude) throughout this time period (see Figure 3, third panel), by more than 15 km in the beginning of this time interval, possibly due to a response to the increased dynamic pressure, which was observed in previous studies (Sánchez-Cano et al., 2017). The Δ(Peak Altitude) fluctuates between $\simeq$ - 10 and 8 km after April 11th.

To gain more focus on the temporal correlation, attempt to untangle the many factors garbled together, and not to attribute causation, we estimated the time-lagged cross correlation between the solar wind particle parameters in Figure 3, the solar irradiance measured with MAVEN Extreme Ultraviolet Monitor (EUVM) (Eparvier et al., 2015), and the ROSE proxies, and we show the time-lagged crossed correlation matrix through the heat map in Figure 5: each element, or correlation value, in the matrix is represented in a cell in the map. There is no strong correlation or anti-correlation between time-series, we are anyway below $|0.5|$ values, however we can use this map as support

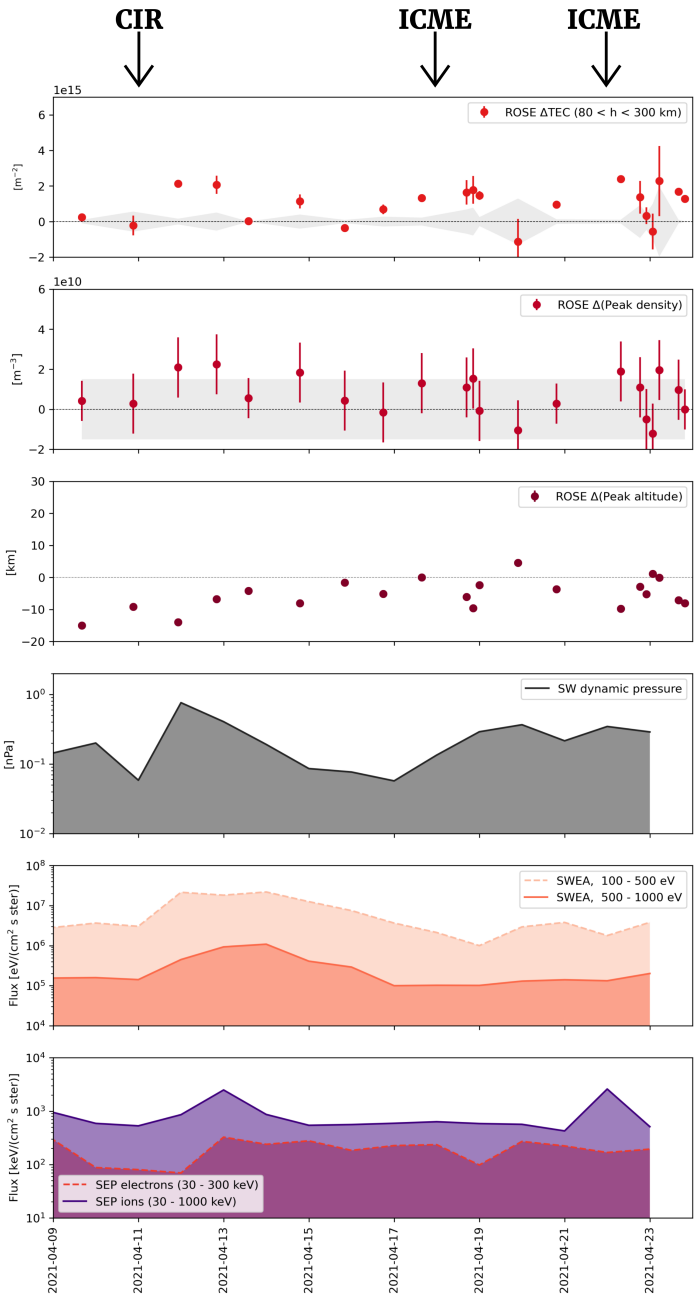

Figure 3: April 2021: From top to bottom, time series of ROSE ΔTEC, ROSE Δ(Peak density), Δ(Peak altitude); solar wind dynamic pressure derived from MAVEN SWIA; SWEA electron flux; SEP ions and electron fluxes. The first three proxies, all derived from ROSE data, are independent from L_S, SZA, and LST, therefore we only report their trend, and we indicate with grey shadows the error estimated as described in Section 2 for each proxy. At the top of the plot we indicate arrival times of the CIR and ICMEs in this time interval as predicted by the ENLIL model.

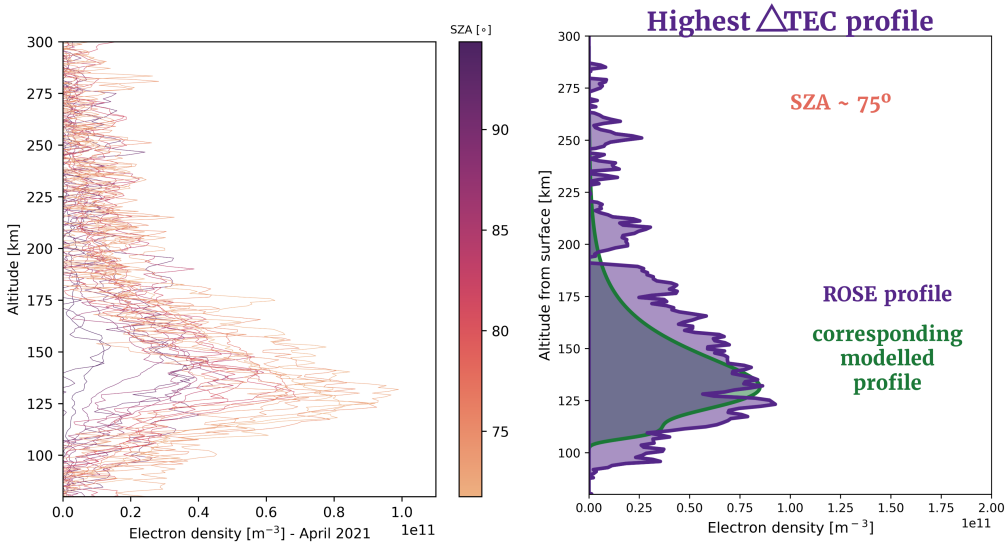

Figure 4: April 2021: (left) ROSE electron density profiles in the time interval covered in Figure 3, with colourscale indicating values SZA: these are the original electron density profiles belonging to **SET A** described in Section 2. (right) ROSE electron density profile that see the highest increase in TEC (purple) compared to the baseline profiles (green).

information to accompany Figure 3: a high clear correlation between two time-series cannot be expected in this case, because there are multiple solar wind parameters modulating the values each single proxy. In other words, solar wind high energy and thermal particles, fields, solar irradiance, these are all affecting the ionosphere: we would not expect to see here a cross correlation = 1 between two time series. However, this matrix can help us see which time series are the most similar to each other more intuitively than Figure 3. It is also important to remind the reader that MAVEN is not upstream, therefore the timing of the in situ parameters may not reflect perfectly the time at which the atmosphere is impacted.

The most similar times-series of parameters and in situ data binned in averaged 12 hours bins, are ΔTEC to SEP electrons time-series, Δ(Peak Density) and to SEP electrons, Δ(Peak Altitude) to EUV 17-22 nm wavelengths and to the solar wind dynamic pressure, and with lag = 0. The most anti-correlated time-series are the Δ(Peak Altitude) to EUV Lyman α with lag = 0, and the Δ(Peak Density) to SWEA 100 - 500 eV: photons with wavelenght $\sim$ 121.6 nm or electrons with energy between 100 - 500 eV might not have enough energy to penetrate down to the main peak. However, electrons with energy between 100 - 500 eV can ionise higher altitudes, while SEP electrons can ionise down to 80 km (the lower limit of our integration).

This might suggest that the ionisation during CIRs and ICME impacts is more spread in altitude and relies on mechanisms additional to photoionisation, differently to what happens in a quiet ionosphere mainly generated by photochemistry, consistently with what (Ulusen et al., 2012; Sánchez-Cano et al., 2019) found.

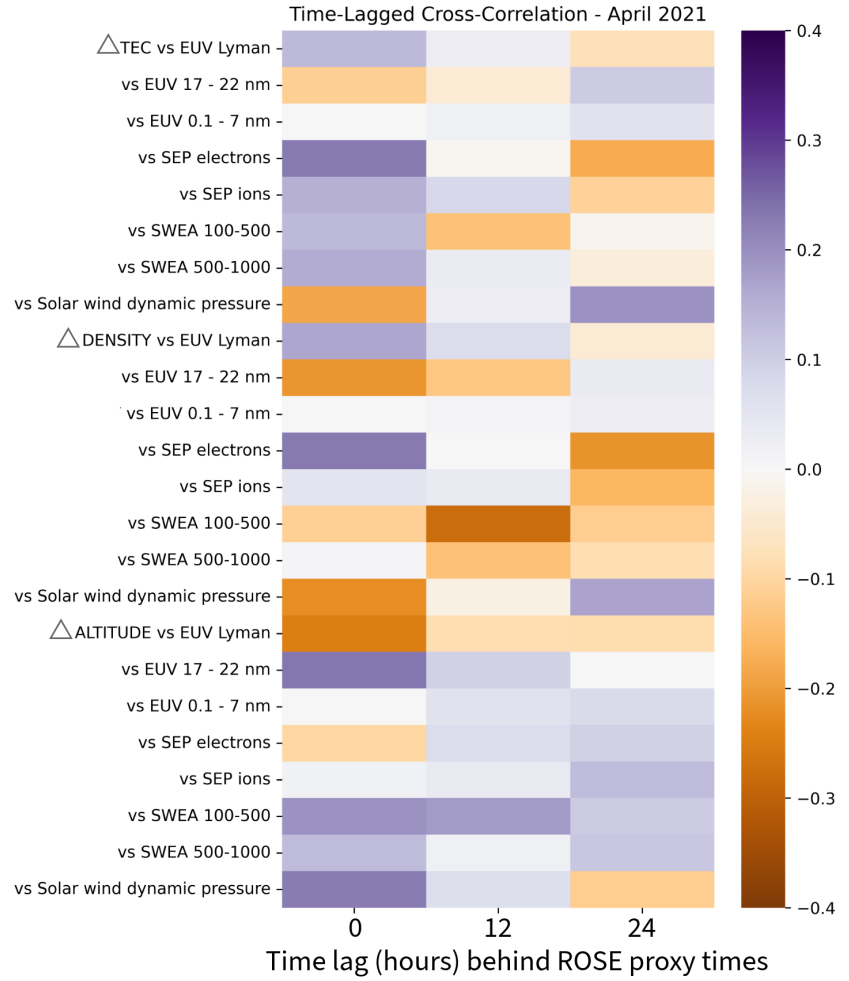

Figure 5: April 2021: Backward time lagged crossed correlation matrix, displayed as a heatmap where, on the y axis, we represent days of lag between the semi-daily averaged solar particles parameters measured by MAVEN in-situ instruments, and the x axis reports the various quantities between which the backward time lagged cross correlation was estimated. The colourscale represent correlation values

3.2. June - July 2022: CIR and ICME impact during dust season and a dust storm

This time interval included 41 electron density profiles collected between June 13th and July 22th 2022, a SZA range between $\simeq$ 47 and 95°. These profiles were collected not only during dust season, but also during dust storms (see Section 1, and Figure 1). In fact, one A storm and one B storm were taking place continuously, overlapping, in the entire time interval under examination (see Section 2). Besides the dust storms lofting the ionosphere from below, in this time interval the ionosphere is also affected by solar events from above: based on the ENLIL simulation results, there may have been an ICME impact at Mars on June 18th, a glancing blow from an ICME combined with a CIR on June 24th, a glancing blow from an ICME on July 2nd, an ICME on July 13th, and a glancing blow from an ICME combined to a CIR on July 14th (see Figure Appendix .12, and arrows on top of Figure 6). MAVEN is upstream of Mars continuously only after July 6th (see Figure Appendix .13).

In Figure 6, we report the three proxies derived from ROSE data, namely ΔTEC, Δ(Peak Density), and Δ(Peak Altitude), then the SW dynamic pressure, then SWEA measurements, and SEP measurements. The SW parameters in this time interval are stronger than during April 2021 (see Figure 3). Definitely, the ionosphere in this time period is subject to significant stress from above and below, and this is reflected in the trends of our three proxies: ΔTEC starts from $\simeq$ 2 $\times 10^{15}$ m^{-2} (one of the maximi values in April 2021) in this time interval and reaches $\simeq$ 5 $\times 10^{15}$ m^{-2} on June 20th, fluctuating between $\simeq$ 4 $\times 10^{15}$ m^{-2} and 0 throughout the rest of this time

interval. Particularly prominent, the increase to $\simeq 4 \times 10^{15}$ m^{-2} on July 22nd, in correspondence to an increase in upstream α density which can be appreciated in Figure Appendix .12.

Δ(Peak Density) is quite elevated from the beginning of the interval, until June 26th, to then proceed to be consistent with 0, or slightly above it, until the end of the interval.

What is dramatically different in June/July 2022 compared to April 2021 is the Δ(Peak Altitude): it fluctuates consistently around values 5-16 km, until July 17th, when it reaches an extraordinary $\sim$ 25 km, and negative values in two instances. These extraordinary 25 km, and other Δ(Peak Altitude) $\sim$ 20 km seem to correspond to a depressed solar wind dynamic pressure. The Δ(Peak Altitude) falling abruptly below 0 might correspond to two profiles collected at SZA $\simeq$ 94 - 95°, possibly reflecting the condition of the nightside ionosphere, not the photochemical dayside ionosphere.

Dust storms can increase the peak altitude up to $\sim$ 20 km (Felici et al., 2020, and references therein), yet the Δ(Peak altitude) ranges between 0 and 16 km, staying on average $\sim$10 km until July 17th, at the end of the time interval examined, when it reaches $>$ 20 km values. These higher values of Δ(Peak altitude) correspond to times at which the solar wind dynamic pressure was lower than the rest of the interval.

Whether or not this specific dust storm would have raised the peak altitudes more if the SW dynamic pressure (see Figure 6) were not as strong in this time interval, is hard to determine with certainty. However, based on the suppressed trend of Δ(Peak Altitude) - negative, on average - during merely CIRs and ICME impacts (see Section 3.1), and previous ob-

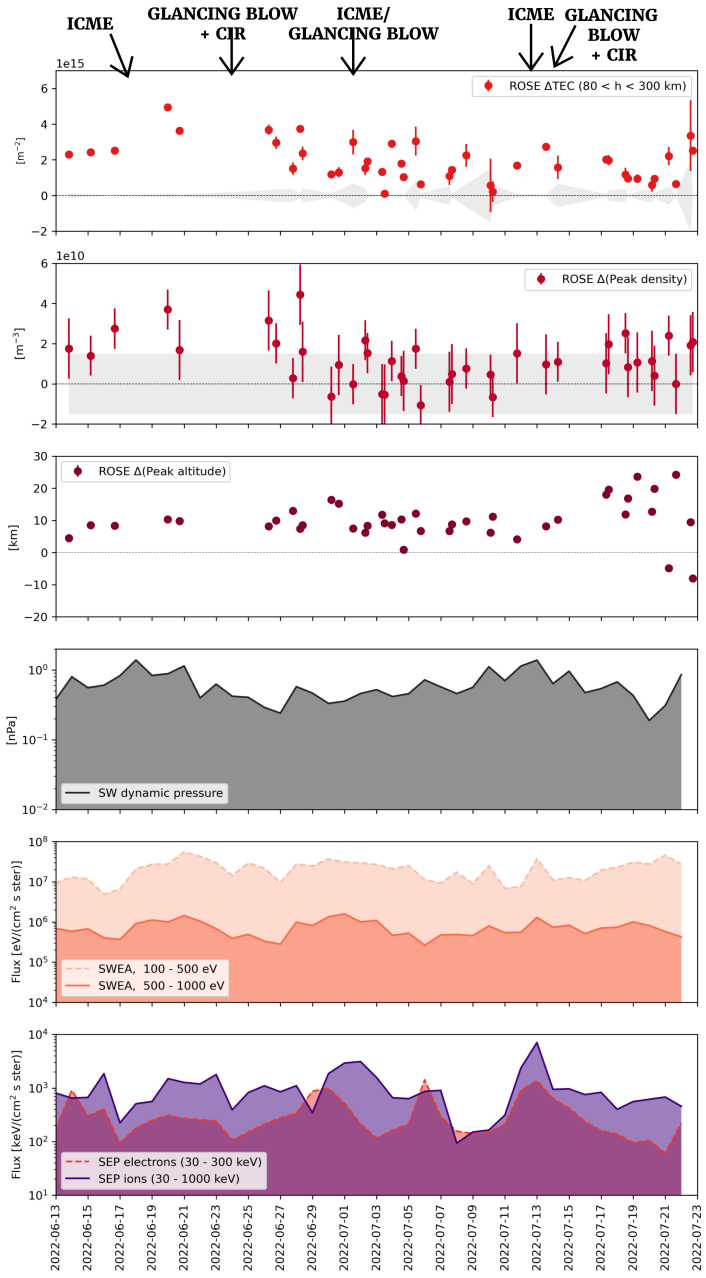

Figure 6: June - July 2022: as Figure 3.

servations collected during dust storms (e.g., Girazian et al., 2019; Felici et al., 2020, and references therein), previously observed suppression of the peak altitude corresponding to higher solar wind dynamic pressure (Sánchez-Cano et al., 2017), we suggest that it might have. To be noted is that part of the increase the peak altitude up to $\sim$ 20 km (e.g., Girazian et al., 2019; Felici et al., 2020, and references theirein) observed might have been due to mere perihelion effects, or dawn vs dusk effects (see Segale et al., https://arxiv.org/abs/2312.00734) not considered in those studies. However, the fact that the high SW dynamic pressure might suppress the raise in peak altitude of the thermosphere during a dust storm could also help explain why Withers and Pratt (2013) found a mere $\simeq$ 5 km increase in peak altitude in the MGS data: during solar maximum, solar activity is higher, therefore there might have been factors from above restraining the loft of the atmosphere induced, from below, by dust.

We report in Figure 7 the series of ROSE electron density profiles for this time period, with colourscale representing SZA (right). We can notice how these profiles are way less noisy than the ones in Figure 4, how pronounced the M1 layer is in some of these profiles (less expected outside of solar maximum Withers et al. (2023)), and how extended to higher and lower altitudes the ionosphere is. The latter point can be further appreciated in Figure 7, right, where we report the ROSE profile that lead to the highest ΔTEC (in purple), with the corresponding modelled profile (green).

As before, we use the time-lagged crossed correlation matrix, displayed in Figure 8 through a heatmap, to help us compare 24h bin averaged time-series trends, with similar caveats to the previous case (e.g. low correlation

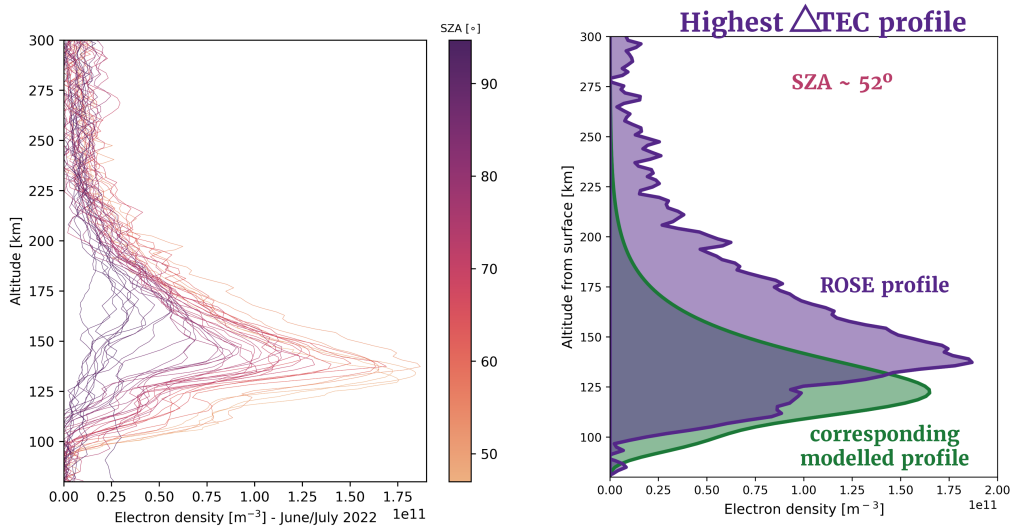

Figure 7: June - July 2022: as Figure 4, for this time interval.

values). In this case, we had to adopt 24h bin size because the 12h bin size, not shown here, resulted in no correlation at all. In this case, ΔTEC time-series is most similar to the SEP electrons time-series with lag = 0. Similarly to what we saw in Figure 5 for April 2021, Δ(Peak density) seems still loosely anti-correlated to lower energy SWEA electrons fluxes (which have energy comparable to the 10 nm photons, though with different cross section). The Δ(Peak altitude) is more correlated with the higher energy SWEA fluxes than for April 2021 for time lag = 0,1,2.

30 of the 41 profiles in this time interval displayed, besides the ever-present-in-the-dayside M2 layer, also the M1 layer (see Figure 7), allowing us to observe how both the M1 and M2 layers, therefore different ionospheric altitudes, respond to a dust storm, while compressed and percolated by solar

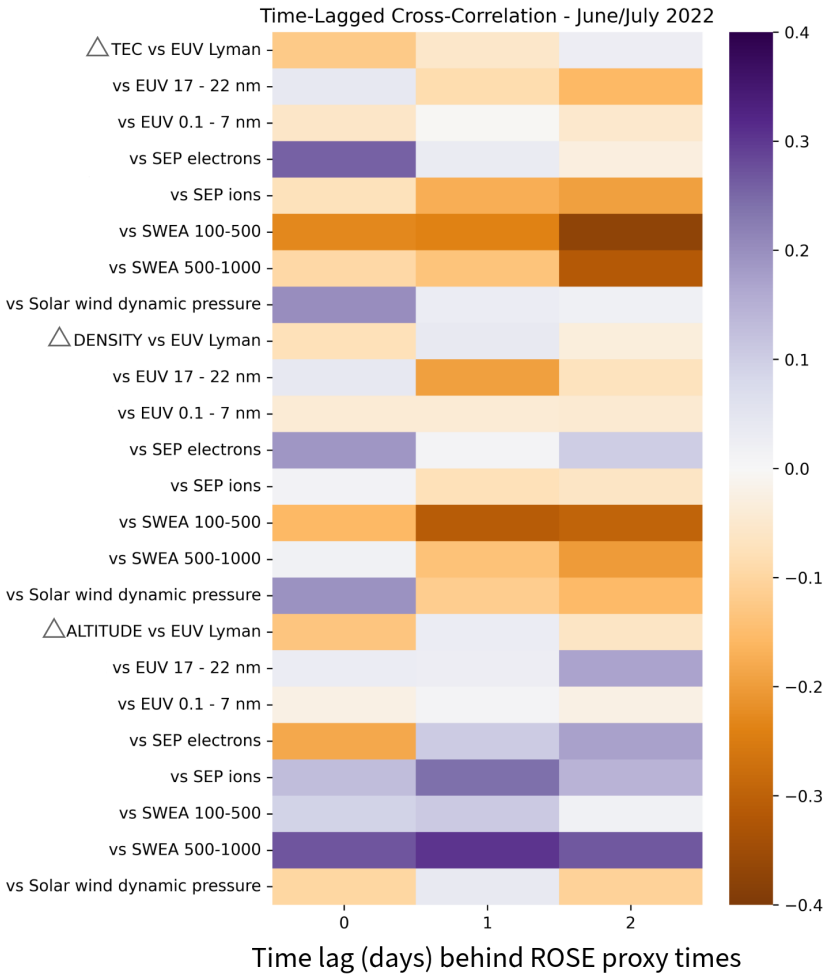

Figure 8: June - July 2022: as Figure 5, for this time interval.

particles and fields. We show in Figure 9(left) the 41 peak altitudes as a function of SZA and ΔTEC, and in Figure 9(right) the altitude of the peak of both layers as a function of SZA, and also the baseline values obtained by Segale et al., [https://arxiv.org/abs/2312.00734] for the ionosphere at dawn and dusk at perihelion: both M2 and M1 peak altitudes are above the baseline expected (but one profile that has a M1 layer as well as the M2, the last in this set and two in total, see Figure 6), indicating that the thermosphere was generally lofted by the dust storm underneath. Moreover, for profiles that display both M1 and M2 layers, the M2 peak altitudes display a distance from their baseline (also reported in Figure 6 bottom panel, as Δ(Peak Altitude)) between -4.9 (only one point has negative value) and 16.8 km, and the M1 between -0.5 and 17.5 km, where these two ranges are consistent within error. This suggests that the M2 and M1 layers are not affected differently by a dust storm: the thermosphere, on average, lofts as a unit.

To add to the global picture of the ionosphere when triggered by solar drivers, aurora enhancement during an ICME was previously detected by Jakosky et al. (2015a). Proton aurora at Mars commonly occur across the entire dayside of the planet around the southern summer solstice (Hughes et al., 2019). This time period overlaps with the Martian dust storm season when atmospheric dust and temperatures reach an annual high, leading to increased atmospheric H escape rates and significant inflation of the hydrogen (H) corona beyond the bow shock, and in turn, more frequent and bright proton aurora activity during this time (Hughes et al., 2019; Chaffin et al., 2021). The Imaging Ultraviolet Spectrograph (IUVS) instrument (McClintock et al., 2015) on board the MAVEN spacecraft observed multiple notable

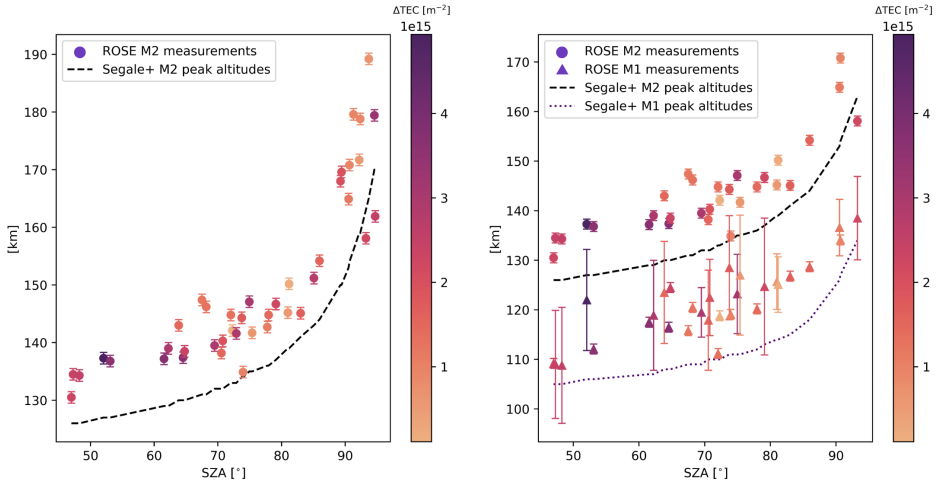

Figure 9: June - July 2022: (Left) All (41) M2 peak altitudes (circles) for the time interval in the timeline in Figure 8, compared to baseline values from their LST time sector and L_S around perihelion reported by Segale et al. [https://arxiv.org/abs/2312.00734 (Right) M2 peak altitudes (circles) and M1 peak altitudes (triangles) for the time interval in the timeline in Figure 8, for the electron density profiles that show both M2 and M1 layers (30), compared to baseline values from their LST time sector and L_S around perihelion reported by Segale et al. [https://arxiv.org/abs/2312.00734] for both layers.

proton aurora events during the months of June and July of 2022 (e.g., Figure 10). These events are observed in the IUVS limb scan data as enhancements in the H Lyman-α (Ly-α) emission (121.6 nm) above the background coronal H brightness. Figure 10 shows an example proton aurora detection during the time period of this study (Orbit 16784 on 13 July 202203:34 UTC). Figure 10 presents a synthetic image format of the un-binned Ly-α limb scan data acquired during the outlimb portion of the MAVEN orbit; i.e., each of the six outlimb IUVS limb scans (horizontally aligned panels) displays the Ly-α intensity for each of the 21 IUVS mirror integrations (vertical) and seven spatial bins within each scan (diagonal/horizontal rectangular bins) (e.g., similar to Figure 2 from Deighan et al. (2018)). Note that although all of the limb scans are displayed side-by-side in the figure, there is actually a spatial separation between each scan. The highest intensity bins in the $\sim$110-150km altitude range correspond with a Ly-α enhancement above the background coronal H that is associated with proton aurora activity. Numerous proton aurora events observed during this time period correspond with increases in the ROSE TEC, peak density, and/or peak altitude, demonstrating the widespread and multifaceted impact of dust activity and extreme solar activity on the dayside of the planet.

4. Summary and conclusions

We utilised the study conducted by Segale et al., [https://arxiv.org/abs/2312.00734] as a baseline for the photochemical Martian ionosphere through solar minimum leading to solar maximum, during dust season, or perihelion season, and aphelion season, and at dawn and dusk, to define three proxies from ROSE

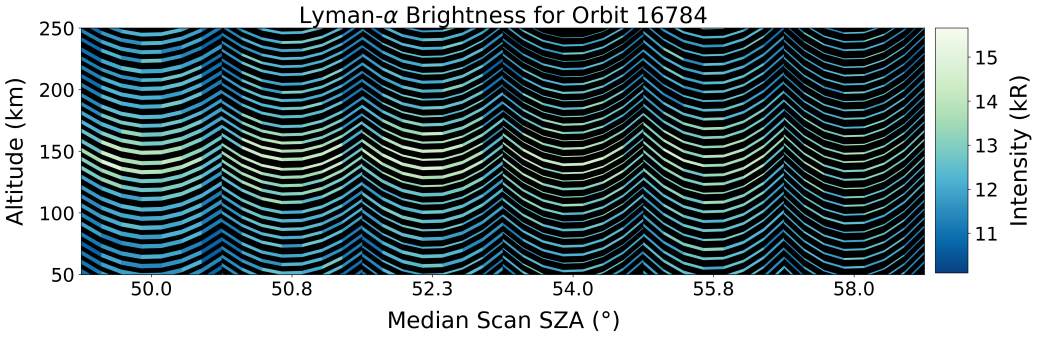

Figure 10: A synthetic image format of IUVS Ly$-\alpha$ intensity (see text for details), showing an enhancement in Ly$-\alpha$ above the background coronal H due to proton aurora activity during this orbit. This IUVS observation was taken during the outlimb portion of the MAVEN orbit (Orbit n.16784 on 13 July 202203:34 UTC), and occurs during the same time period as the ROSE observations shown in Figure 6, corresponding to a local maximum in ΔTEC, demonstrating the widespread effect of dust activity and extreme solar activity on the dayside of the planet.

electron density profiles - ΔTEC, Δ(Peak Density), and Δ(Peak Altitude). The purpose of defining these three proxies is to estimate the deviations from a photochemical ionosphere when the ionosphere is subject to external drivers, such as CIRs, ICMEs, and dust storms. In fact, we used these three proxies to study the response to solar events that hit Mars at aphelion and during dust storms. While there are too many different factors at play to be able to make definitive statements about causality from the analysis of only two time periods, this study suggests that:

1. an increase in SEP particles flux (seen with MAVEN SEP) can correspond to an increase in ionisation down to 80 km altitudes, with a short (< 1 day) thermospheric response, increasing the TEC between 80 and 300 km altitude up to $\simeq 2.5 \times 10^{15}$ m^{-2} in April 2021 and up to $\simeq 5$

$\times 10^{15}$ m^{-2} in June/July 2022. An increase in electron fluxes detected with SWEA can correspond in time to an increase in the altitude at which highest electron density is measured.

2. in June/July 2022, an A storm and a B storm were ongoing and merging under the ionosphere throughout the time period we examined. From 31 profiles that showed both the M2 and M1 layer, we observe that, on average, M1 and M2 peak altitudes raise the same amount, suggesting that the thermosphere might loft as a unit. Whether or not high SW dynamic pressure suppresses the raise of the peak altitudes is harder to determine, however, comparisons between the Δ(Peak Altitude) in April 2021 and the Δ(Peak Altitude) in June/July 2022, and with results from previous studies suggest that that might be the case.
3. this time period corresponds to the detection of several proton aurora events, detected with MAVEN IUVS, of which the brightness modulates as well as ROSE TEC, peak density, and/or peak altitude do, underlining how complex and multifaceted the impact of dust activity and extreme solar activity on the Martian ionosphere can be.

The approaching of solar maximum, and of dust season during solar maximum, will provide us with more opportunities to conduct systematic and statistical studies of the impact of solar events on the Martian ionosphere with or without dust storm lofting the thermosphere, coupled with future proton aurora studies.

Acknowledgements

This work was supported by NASA under award number NNH1OCCO4C, LASP subcontract 9500306435. MAVEN key parameters data bundle available on https://pds-ppi.igpp.ucla.edu/search/view/?f=yes&id=pds://PPI/maven.insitu.calibrated Simulation results have been provided by the Community Coordinated Modeling Center (CCMC) at Goddard Space Flight Center through their publicly available simulation services (`https://ccmc.gsfc.nasa.gov`). The ENLIL Model was developed by Dusan Odstrcil, at George Mason University.

Appendix A

April 2021

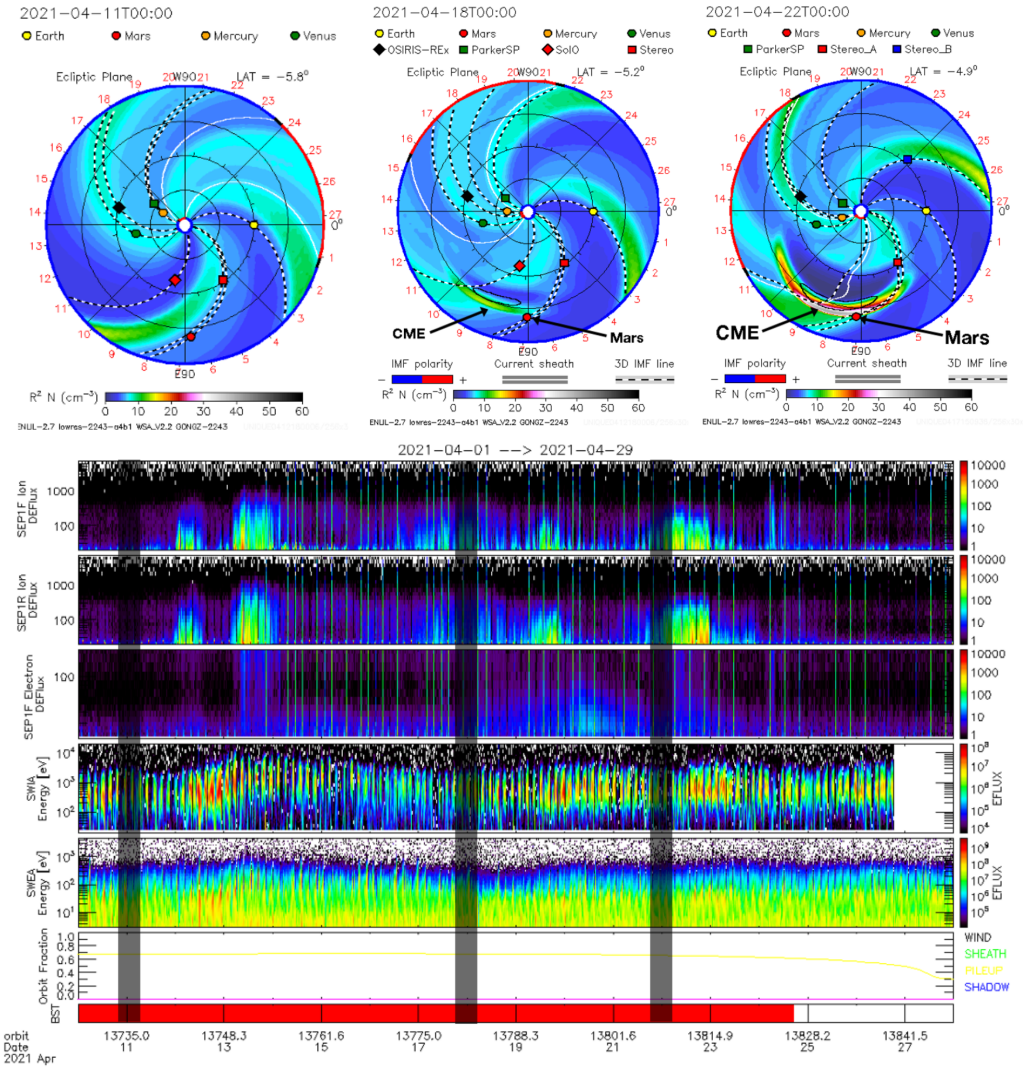

Figure Appendix .11: April 2021: heliospheric conditions results of ENLIL runs for this time period (top); MAVEN in situ SEP and SWEA measurements. We highlighted with black shadows predicted solar events arrival time.

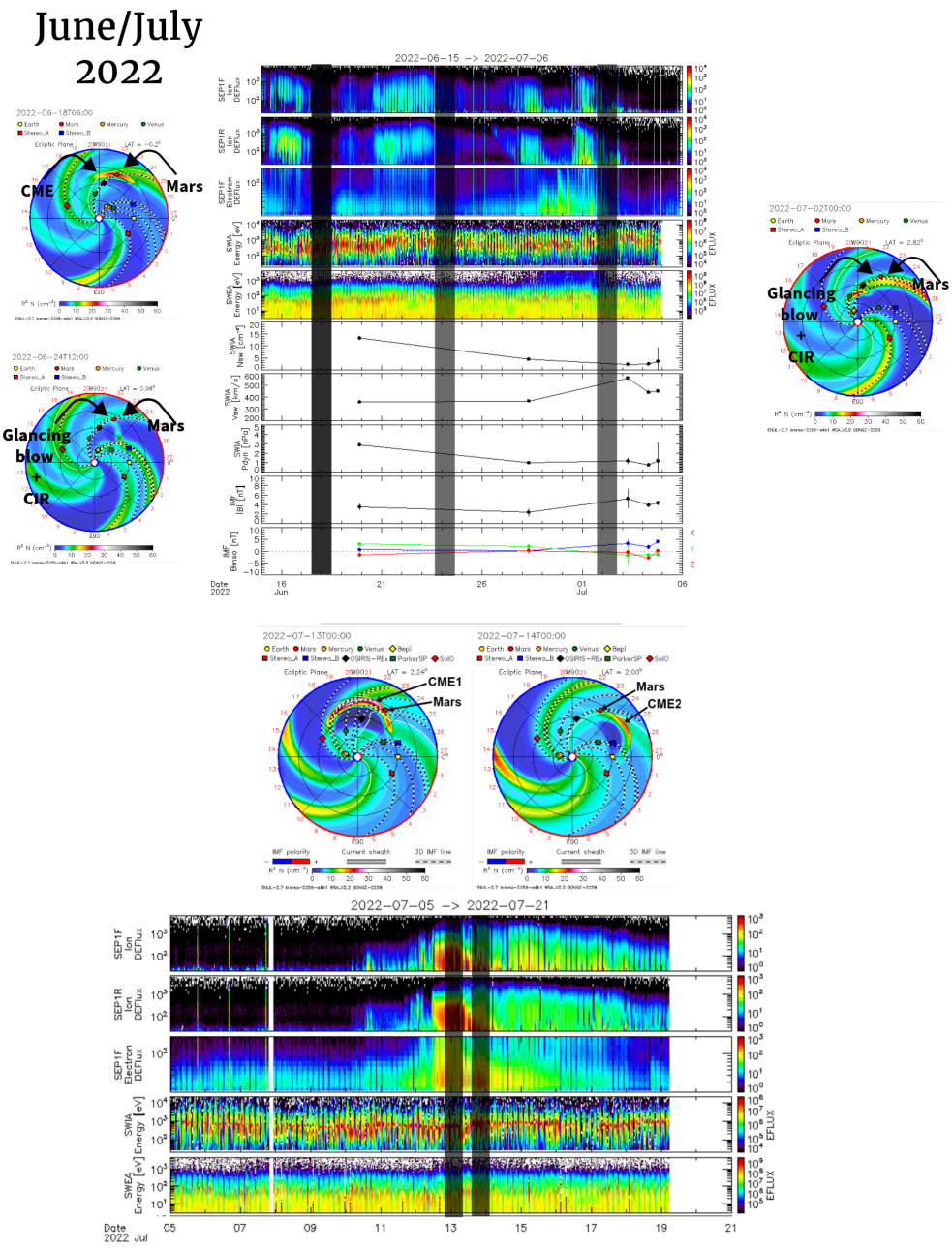

Figure Appendix .12: June/July 2022: as Figure Appendix .11, but for this time period.

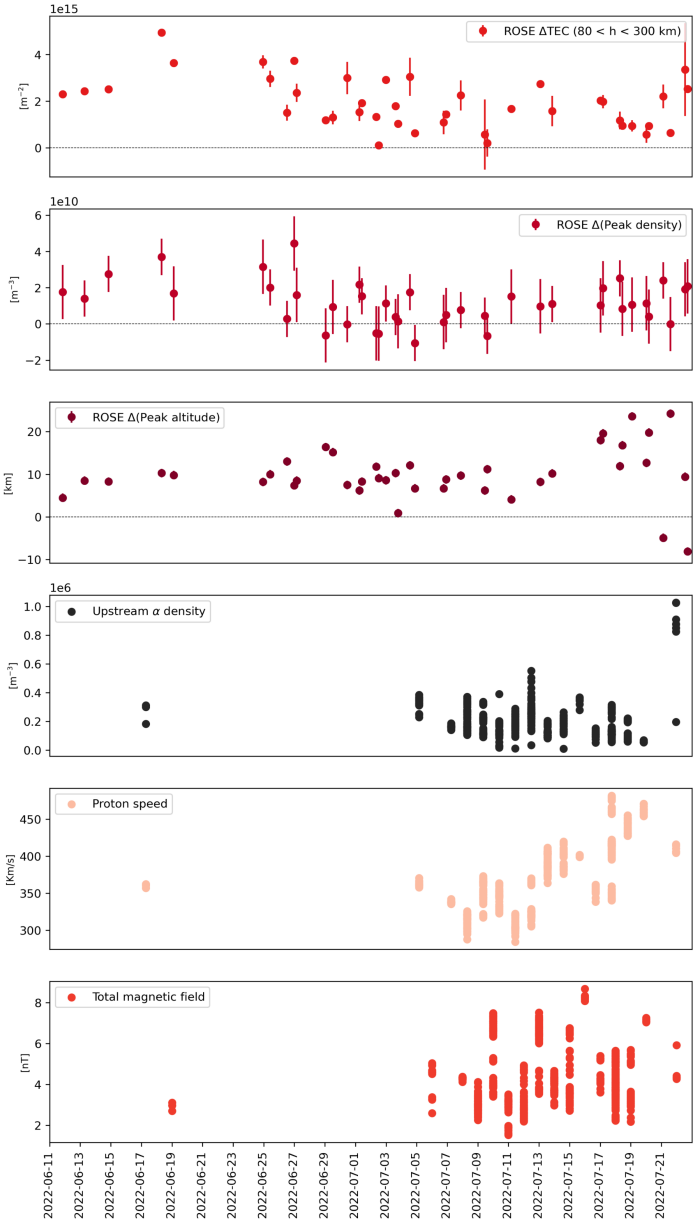

Figure Appendix .13: June/July 2022: as Figure 3 for the top three panels. The bottom three panels show MAVEN upstream high resolution data only for α density, proton speed, and SW total magnetic field (Halekas et al., 2015; Halekas et al., 2017, 2015), available at `https://homepage.physics.uiowa.edu/~jhalekas/drivers.html`.

References

Barth, C., I. F. Stewart, A., Bougher, S.W., M. Hunten, D., Bauer, S., Nagy, A., 1992. Aeronomy of the Current Martian Atmosphere.

Bougher, S.W., Brain, D.A., Fox, J.L., Francisco, G.G., Simon-Wedlund, C., Withers, P.G., 2017. Upper Neutral Atmosphere and Ionosphere. Cambridge University Press. Cambridge Planetary Science, pp. 433–463. doi:10.1017/9781139060172.014.

Chaffin, M.S., Kass, D.M., Aoki, S., Fedorova, A.A., Deighan, J., Connour, K., Heavens, N.G., Kleinböhl, A., Jain, S.K., Chaufray, J.Y., Mayyasi, M., Clarke, J.T., Stewart, A.I.F., Evans, J.S., Stevens, M.H., McClintock, W.E., Crismani, M.M.J., Holsclaw, G.M., Lefevre, F., Lo, D.Y., Montmessin, F., Schneider, N.M., Jakosky, B., Villanueva, G., Liuzzi, G., Daerden, F., Thomas, I.R., Lopez-Moreno, J.J., Patel, M.R., Bellucci, G., Ristic, B., Erwin, J.T., Vandaele, A.C., Trokhimovskiy, A., Korablev, O.I., 2021. Martian water loss to space enhanced by regional dust storms. Nature Astronomy 5, 1036–1042. URL: https://doi.org/10.1038/s41550-021-01425-w, doi:10.1038/s41550-021-01425-w.

Chamberlain, J., Hunten, D., 1987. Theory of Planetary Atmospheres. second ed. ed., Academic Press, New York.

Deighan, J., Jain, S.K., Chaffin, M.S., Fang, X., Halekas, J.S., Clarke, J.T., Schneider, N.M., Stewart, A.I.F., Chaufray, J.Y., Evans, J.S., Stevens, M.H., Mayyasi, M., Stiepen, A., Crismani, M., McClintock, W.E., Holsclaw, G.M., Lo, D.Y., Montmessin, F., Lefèvre, F., Jakosky,

B.M., 2018. Discovery of a proton aurora at Mars. Nature Astronomy 2, 802–807. URL: https://doi.org/10.1038/s41550-018-0538-5, doi:10.1038/s41550-018-0538-5.

Dresing, N., Rodríguez-García, L., Jebaraj, I.C., Warmuth, A., Wallace, S., Balmaceda, L., Podladchikova, T., Strauss, R.D., Kouloumvakos, A., Palmroos, C., Krupar, V., Gieseler, J., Xu, Z., Mitchell, J.G., Cohen, C.M.S., de Nolfo, G.A., Palmerio, E., Carcaboso, F., Kilpua, E.K.J., Trotta, D., Auster, U., Asvestari, E., da Silva, D., Dröge, W., Getachew, T., Gómez-Herrero, R., Grande, M., Heyner, D., Holmström, M., Huovelin, J., Kartavykh, Y., Laurenza, M., Lee, C.O., Mason, G., Maksimovic, M., Mieth, J., Murakami, G., Oleynik, P., Pinto, M., Pulupa, M., Richter, I., Rodríguez-Pacheco, J., Sánchez-Cano, B., Schuller, F., Ueno, H., Vainio, R., Vecchio, A., Veronig, A.M., Wijsen, N., 2023. The 17 April 2021 widespread solar energetic particle event. A&A 674. URL: https://doi.org/10.1051/0004-6361/202345938.

Dubinin, E., Fraenz, M., Woch, J., Duru, F., Gurnett, D., Modolo, R., Barabash, S., Lundin, R., 2009. Ionospheric storms on Mars: Impact of the corotating interaction region. Geophysical Research Letters 36. URL: https://doi.org/10.1029/2008GL036559, doi:https://doi.org/10.1029/2008GL036559.

Edberg, N.J.T., Nilsson, H., Williams, A.O., Lester, M., Milan, S.E., Cowley, S.W.H., Fränz, M., Barabash, S., Futaana, Y., 2010. Pumping out the atmosphere of Mars through solar wind pressure pulses. Geophysical

Research Letters 37. URL: https://doi.org/10.1029/2009GL041814, doi:https://doi.org/10.1029/2009GL041814.

Ehresmann, B., Hassler, D.M., Zeitlin, C., Guo, J., Wimmer-Schweingruber, R.F., Matthiä, D., Lohf, H., Burmeister, S., Rafkin, S.C.R., Berger, T., Reitz, G., 2018. Energetic particle radiation environment observed by rad on the surface of mars during the september 2017 event. Geophysical Research Letters 45, 5305–5311. URL: https://doi.org/10.1029/2018GL077801, doi:https://doi.org/10.1029/2018GL077801.

Eparvier, F.G., Chamberlin, P.C., Woods, T.N., Thiemann, E.M.B., 2015. The solar extreme ultraviolet monitor for MAVEN. Space Science Reviews 195, 293–301. URL: https://doi.org/10.1007/s11214-015-0195-2, doi:10.1007/s11214-015-0195-2.

Fallows, K., Withers, P., Matta, M., 2015. An observational study of the influence of solar zenith angle on properties of the M1 layer of the Mars ionosphere. J. Geophys. Res. 120, 1299–1310. doi:10.1002/2014JA020750.

Felici, M., Withers, P., Smith, M.D., González-Galindo, F., Oudrhiri, K., Kahan, D., 2020. MAVEN ROSE Observations of the Response of the Martian Ionosphere to Dust Storms. Journal of Geophysical Research 125, e27083. doi:10.1029/2019JA027083.

Fox, J.L., 2004. Response of the Martian thermosphere/ionosphere to enhanced fluxes of solar soft X rays. Journal of Geophysical Research: Space Physics 109. URL: https://doi.org/10.1029/2004JA010380, doi:10.1029/2004JA010380.

Girazian, Z., Luppen, Z., Morgan, D.D., Chu, F., Montabone, L., Thiemann, E.M.B., Gurnett, D.A., Halekas, J., Kopf, A.J., Nemec, F., 2019. Variations in the ionospheric peak altitude at mars in response to dust storms: 13 years of observations from the mars express radar sounder. arXiv:1906.07111.

Halekas, J.S., Lillis, R.J., Mitchell, D.L., Cravens, T.E., Mazelle, C., Connerney, J.E.P., Espley, J.R., Mahaffy, P.R., Benna, M., Jakosky, B.M., Luhmann, J.G., McFadden, J.P., Larson, D.E., Harada, Y., Ruhunusiri, S., 2015. MAVEN observations of solar wind hydrogen deposition in the atmosphere of Mars. Geophysical Research Letters 42, 8901–8909. URL: https://doi.org/10.1002/2015GL064693, doi:https://doi.org/10.1002/2015GL064693.

Halekas, J.S., Ruhunusiri, S., Harada, Y., Collinson, G., Mitchell, D.L., Mazelle, C., McFadden, J.P., Connerney, J.E.P., Espley, J.R., Eparvier, F., Luhmann, J.G., Jakosky, B.M., 2017. Structure, dynamics, and seasonal variability of the Mars-solar wind interaction: MAVEN Solar Wind Ion Analyzer in-flight performance and science results. Journal of Geophysical Research: Space Physics 122, 547–578. URL: https://doi.org/10.1002/2016JA023167, doi:https://doi.org/10.1002/2016JA023167.

Halekas, J.S., Taylor, E.R., Dalton, G., Johnson, G., Curtis, D.W., McFadden, J.P., Mitchell, D.L., Lin, R.P., Jakosky, B.M., 2015. The Solar Wind Ion Analyzer for MAVEN. Space Sci. Rev. 195, 125–151. doi:10.1007/s11214-013-0029-z.

Harada, Y., Nakamura, Y., Sánchez-Cano, B., Lester, M., Terada, N.,

Leblanc, F., 2023. Radio Absorption in the Nightside Ionosphere of Mars During Solar Energetic Particle Events. Space Weather 21, e2023SW003755. URL: https://doi.org/10.1029/2023SW003755, doi:https://doi.org/10.1029/2023SW003755.

Hughes, A., Chaffin, M., Mierkiewicz, E., Deighan, J., Jain, S., Schneider, N., Mayyasi, M., Jakosky, B., 2019. Proton Aurora on Mars: A Dayside Phenomenon Pervasive in Southern Summer. Journal of Geophysical Research: Space Physics 124, 10533–10548. URL: https://doi.org/10.1029/2019JA027140, doi:https://doi.org/10.1029/2019JA027140.

Jakosky, B.M., Grebowsky, J.M., Luhmann, J.G., Connerney, J., Eparvier, F., Ergun, R., Halekas, J., Larson, D., Mahaffy, P., McFadden, J., Mitchell, D.L., Schneider, N., Zurek, R., Bougher, S., Brain, D., Ma, Y.J., Mazelle, C., Andersson, L., Andrews, D., Baird, D., Baker, D., Bell, J.M., Benna, M., Chaffin, M., Chamberlin, P., Chaufray, Y.Y., Clarke, J., Collinson, G., Combi, M., Crary, F., Cravens, T., Crismani, M., Curry, S., Curtis, D., Deighan, J., Delory, G., Dewey, R., DiBraccio, G., Dong, C., Dong, Y., Dunn, P., Elrod, M., England, S., Eriksson, A., Espley, J., Evans, S., Fang, X., Fillingim, M., Fortier, K., Fowler, C.M., Fox, J., Gröller, H., Guzewich, S., Hara, T., Harada, Y., Holsclaw, G., Jain, S.K., Jolitz, R., Leblanc, F., Lee, C.O., Lee, Y., Lefevre, F., Lillis, R., Livi, R., Lo, D., Mayyasi, M., McClintock, W., McEnulty, T., Modolo, R., Montmessin, F., Morooka, M., Nagy, A., Olsen, K., Peterson, W., Rahmati, A., Ruhunusiri, S., Russell, C.T., Sakai, S., Sauvaud, J.A., Seki, K., Steckiewicz, M., Stevens, M., Stewart, A.I.F., Stiepen,

A., Stone, S., Tenishev, V., Thiemann, E., Tolson, R., Toublanc, D., Vogt, M., Weber, T., Withers, P., Woods, T., Yelle, R., 2015a. MAVEN observations of the response of Mars to an interplanetary coronal mass ejection. Science 350, aad0210. URL: https://www.science.org/doi/abs/10.1126/science.aad0210, doi:10.1126/science.aad0210, arXiv:https://www.science.org/doi/pdf/10.1126/science.aad0210.

Jakosky, B.M., Lin, R.P., Grebowsky, J.M., Luhmann, J.G., Mitchell, D.F., Beutelschies, G., Priser, T., Acuna, M., Andersson, L., Baird, D., Baker, D., Bartlett, R., Benna, M., Bougher, S., Brain, D., Carson, D., Cauffman, S., Chamberlin, P., Chaufray, J.Y., Cheatom, O., Clarke, J., Connerney, J., Cravens, T., Curtis, D., Delory, G., Demcak, S., DeWolfe, A., Eparvier, F., Ergun, R., Eriksson, A., Espley, J., Fang, X., Folta, D., Fox, J., Gomez-Rosa, C., Habenicht, S., Halekas, J., Holsclaw, G., Houghton, M., Howard, R., Jarosz, M., Jedrich, N., Johnson, M., Kasprzak, W., Kelley, M., King, T., Lankton, M., Larson, D., Leblanc, F., Lefevre, F., Lillis, R., Mahaffy, P., Mazelle, C., McClintock, W., McFadden, J., Mitchell, D.L., Montmessin, F., Morrissey, J., Peterson, W., Possel, W., Sauvaud, J.A., Schneider, N., Sidney, W., Sparacino, S., Stewart, A.I.F., Tolson, R., Toublanc, D., Waters, C., Woods, T., Yelle, R., Zurek, R., 2015b. The Mars Atmosphere and Volatile Evolution (MAVEN) Mission. Space Science Reviews 195, 3–48. URL: https://doi.org/10.1007/s11214-015-0139-x, doi:10.1007/s11214-015-0139-x.

Jones, S.R., Scott, C.J., Barnard, L.A., Highfield, R., Lintott, C.J., Baeten, E., 2020. The Visual Complexity of Coronal Mass Ejections Follows the

Solar Cycle. Space Weather 18, e2020SW002556. URL: https://doi.org/10.1029/2020SW002556, doi:https://doi.org/10.1029/2020SW002556.

Kahre, M.A., Murphy, J.R., Newman, C.E., Wilson, R.J., Cantor, B.A., Lemmon, M.T., Wolff, M.J., 2017. The Mars Dust Cycle. pp. 229–294. URL: https://ui.adsabs.harvard.edu/abs/2017acm..book..229K, doi:10.1017/9781139060172.010.

Kass, D.M., Kleinböhl, A., McCleese, D.J., Schofield, J.T., Smith, M.D., 2016. Interannual similarity in the martian atmosphere during the dust storm season. Geophysical Research Letters 43, 6111–6118. URL: https://doi.org/10.1002/2016GL068978, doi:10.1002/2016GL068978.

Larson, D.E., Lillis, R.J., Lee, C.O., Dunn, P.A., Hatch, K., Robinson, M., Glaser, D., Chen, J., Curtis, D., Tiu, C., Lin, R.P., Luhmann, J.G., Jakosky, B.M., 2015. The MAVEN Solar Energetic Particle Investigation. Space Sci. Rev. 195, 153–172. doi:10.1007/s11214-015-0218-z.

Lee, C.O., Jakosky, B.M., Luhmann, J.G., Brain, D.A., Mays, M.L., Hassler, D.M., Holmström, M., Larson, D.E., Mitchell, D.L., Mazelle, C., Halekas, J.S., 2018. Observations and Impacts of the 10 September 2017 Solar Events at Mars: An Overview and Synthesis of the Initial Results. Geophysical Research Letters 45, 8871–8885. URL: https://doi.org/10.1029/2018GL079162, doi:https://doi.org/10.1029/2018GL079162.

Leovy, C., 2001. Weather and climate on Mars. Nature 412, 245–249. URL: https://ui.adsabs.harvard.edu/abs/2001Natur.412..245L.

Lester, M., Sanchez-Cano, B., Potts, D., Lillis, R., Cartacci, M., Bernardini, F., Orosei, R., Perry, M., Putzig, N., Campbell, B., Blelly, P.L., Milan, S., Opgenoorth, H., Witasse, O., Redrojo, E.M.M., Russell, A., 2022. The Impact of Energetic Particles on the Martian Ionosphere During a Full Solar Cycle of Radar Observations: Radar Blackouts. Journal of Geophysical Research: Space Physics 127, e2021JA029535. URL: https://doi.org/10.1029/2021JA029535, doi:https://doi.org/10.1029/2021JA029535.

McClintock, W.E., Schneider, N.M., Holsclaw, G.M., Clarke, J.T., Hoskins, A.C., Stewart, I., Montmessin, F., Yelle, R.V., Deighan, J., 2015. The Imaging Ultraviolet Spectrograph (IUVS) for the MAVEN Mission. Space Science Reviews 195, 75–124. URL: https://doi.org/10.1007/s11214-014-0098-7, doi:10.1007/s11214-014-0098-7.

Mitchell, D.L., Mazelle, C., Sauvaud, J.A., Thocaven, J.J., Rouzaud, J., Fedorov, A., Rouger, P., Toublanc, D., Taylor, E., Gordon, D., Robinson, M., Heavner, S., Turin, P., Diaz-Aguado, M., Curtis, D.W., Lin, R.P., Jakosky, B.M., 2016. The MAVEN Solar Wind Electron Analyzer. Space Sci. Rev. 200, 495–528. doi:10.1007/s11214-015-0232-1.

Montabone, L., Forget, F., Millour, E., Wilson, R.J., Lewis, S.R., Cantor, B., Kass, D., Kleinböhl, A., Lemmon, M.T., Smith, M.D., Wolff, M.J., 2015. Eight-year climatology of dust optical depth on mars. Icarus 251, 65–95. URL: http://www.sciencedirect.com/science/article/pii/S0019103515000044, doi:https://doi.org/10.1016/j.icarus.2014.12.034.

Montabone, L., Spiga, A., Kass, D.M., Kleinböhl, A., Forget, F., Millour,

E., 2020. Martian year 34 column dust climatology from mars climate sounder observations: Reconstructed maps and model simulations. Journal of Geophysical Research: Planets n/a, e2019JE006111. URL: https://doi.org/10.1029/2019JE006111, doi:10.1029/2019JE006111.

Morgan, D.D., Diéval, C., Gurnett, D.A., Duru, F., Dubinin, E.M., Fränz, M., Andrews, D.J., Opgenoorth, H.J., Uluşen, D., Mitrofanov, I., Plaut, J.J., 2014. Effects of a strong ICME on the Martian ionosphere as detected by Mars Express and Mars Odyssey. Journal of Geophysical Research: Space Physics 119, 5891–5908. URL: https://doi.org/10.1002/2013JA019522, doi:https://doi.org/10.1002/2013JA019522.

Nakamura, Y., Terada, N., Leblanc, F., Rahmati, A., Nakagawa, H., Sakai, S., Hiruba, S., Kataoka, R., Murase, K., 2022. Modeling of Diffuse Auroral Emission at Mars: Contribution of MeV Protons. Journal of Geophysical Research: Space Physics 127, e2021JA029914. URL: https://doi.org/10.1029/2021JA029914, doi:https://doi.org/10.1029/2021JA029914.

Odstrcil, D., 2003. Modeling 3-D solar wind structure. Advances in Space Research 32, 497–506. URL: https://www.sciencedirect.com/science/article/pii/S0273117703003326, doi:https://doi.org/10.1016/S0273-1177(03)00332-6.

Opgenoorth, H.J., Andrews, D.J., Fränz, M., Lester, M., Edberg, N.J.T., Morgan, D., Duru, F., Witasse, O., Williams, A.O., 2013. Mars ionospheric response to solar wind variability. Journal of Geophysical Research: Space Physics 118, 6558–6587. URL: https://doi.org/10.1002/jgra.50537, doi:https://doi.org/10.1002/jgra.50537.

Owens, M.J., 2018. Solar Wind and Heavy Ion Properties of Interplanetary Coronal Mass Ejections. Solar Physics 293, 122. URL: https://doi.org/10.1007/s11207-018-1343-0, doi:10.1007/s11207-018-1343-0.

Palmerio, E., Kilpua, E.K.J., Witasse, O., Barnes, D., Sánchez-Cano, B., Weiss, A.J., Nieves-Chinchilla, T., Möstl, C., Jian, L.K., Mierla, M., Zhukov, A.N., Guo, J., Rodriguez, L., Lowrance, P.J., Isavnin, A., Turc, L., Futaana, Y., Holmström, M., 2021. CME Magnetic Structure and IMF Preconditioning Affecting SEP Transport. Space Weather 19, e2020SW002654. URL: https://doi.org/10.1029/2020SW002654, doi:https://doi.org/10.1029/2020SW002654.

Peter, K., Pätzold, M., Molina-Cuberos, G.J., González-Galindo, F., Witasse, O., Tellmann, S., Häusler, B., Bird, M.K., 2021. The lower dayside ionosphere of Mars from 14 years of MaRS radio science observations. Icarus 359, 114213. URL: https://www.sciencedirect.com/science/article/pii/S0019103520305455, doi:https://doi.org/10.1016/j.icarus.2020.114213.

Ram, L., Rout, D., Rathi, R., Mondal, S., Sarkhel, S., Halekas, J., 2023. A Comparison of the Impacts of CMEs and CIRs on the Martian Dayside and Nightside Ionospheric Species. Journal of Geophysical Research: Planets 128, e2022JE007649. URL: https://doi.org/10.1029/2022JE007649, doi:https://doi.org/10.1029/2022JE007649.

Richardson, I.G., 2018. Solar wind stream interaction regions throughout the heliosphere. Living Reviews in Solar Physics 15, 1. URL: https://doi.org/10.1007/s41116-017-0011-z, doi:10.1007/s41116-017-0011-z.

Sánchez-Cano, B., Blelly, P.L., Lester, M., Witasse, O., Cartacci, M., Orosei, R., Opgenoorth, H., Lillis, R., Leblanc, F., Milan, S.E., Conroy, P., Floury, N., Plane, J.M.C., Cicchetti, A., Noschese, R., Kopf, A.J., 2019. Origin of the Extended Mars Radar Blackout of September 2017. Journal of Geophysical Research: Space Physics 124, 4556–4568. URL: https://doi.org/10.1029/2018JA026403, doi:https://doi.org/10.1029/2018JA026403.

Sánchez-Cano, B., Hall, B.E.S., Lester, M., Mays, M.L., Witasse, O., Ambrosi, R., Andrews, D., Cartacci, M., Cicchetti, A., Holmström, M., Imber, S., Kajdič, P., Milan, S.E., Noschese, R., Odstrcil, D., Opgenoorth, H., Plaut, J., Ramstad, R., Reyes-Ayala, K.I., 2017. Mars plasma system response to solar wind disturbances during solar minimum. Journal of Geophysical Research: Space Physics 122, 6611–6634. URL: https://doi.org/10.1002/2016JA023587, doi:https://doi.org/10.1002/2016JA023587.

Ulusen, D., Brain, D.A., Luhmann, J.G., Mitchell, D.L., 2012. Investigation of Mars' ionospheric response to solar energetic particle events. Journal of Geophysical Research: Space Physics 117. URL: https://doi.org/10.1029/2012JA017671, doi:https://doi.org/10.1029/2012JA017671.

Withers, P., 2009. A review of observed variability in the dayside ionosphere of Mars. Advances in Space Research 44, 277–307. URL: http://www.sciencedirect.com/science/article/pii/S0273117709002944, doi:https://doi.org/10.1016/j.asr.2009.04.027.

Withers, P., Felici, M., Hensley, K., Mendillo, M., Barbinis, E., Kahan, D., Oudrhiri, K., Girazian, Z., 2023. The ionosphere of Mars from solar minimum to solar maximum: Dayside electron densities from MAVEN and Mars Global Surveyor radio occultations. Icarus 393, 114508. URL: https://www.sciencedirect.com/science/article/pii/S0019103521001834, doi:https://doi.org/10.1016/j.icarus.2021.114508.

Withers, P., Felici, M., Mendillo, M., Moore, L., Narvaez, C., Vogt, M.F., Jakosky, B.M., 2018. First Ionospheric Results From the MAVEN Radio Occultation Science Experiment (ROSE). Journal of Geophysical Research: Space Physics 123, 4171–4180. URL: https://doi.org/10.1029/2018JA025182, doi:doi:10.1029/2018JA025182.

Withers, P., Felici, M., Mendillo, M., Moore, L., Narvaez, C., Vogt, M.F., Oudrhiri, K., Kahan, D., Jakosky, B.M., 2020. The maven radio occultation science experiment (rose). Space Science Reviews 216, 61. URL: https://doi.org/10.1007/s11214-020-00687-6, doi:10.1007/s11214-020-00687-6.

Withers, P., Pratt, R., 2013. An observational study of the response of the upper atmosphere of Mars to lower atmospheric dust storms. Icarus 225, 378–389. doi:10.1016/j.icarus.2013.02.032.

Zeitlin, C., Hassler, D.M., Guo, J., Ehresmann, B., Wimmer-Schweingruber, R.F., Rafkin, S.C.R., Freiherr von Forstner, J.L., Lohf, H., Berger, T., Matthiae, D., Reitz, G., 2018. Analysis of the Radiation Hazard Observed by RAD on the Surface of Mars During the September

2017 Solar Particle Event. Geophysical Research Letters 45, 5845–5851. URL: https://doi.org/10.1029/2018GL077760, doi:https://doi.org/10.1029/2018GL077760.

Zurbuchen, T.H., Richardson, I.G., 2006. In-Situ Solar Wind and Magnetic Field Signatures of Interplanetary Coronal Mass Ejections. Space Science Reviews 123, 31–43. URL: https://doi.org/10.1007/s11214-006-9010-4, doi:10.1007/s11214-006-9010-4.